Research Square

Preprints are preliminary reports that have not undergone peer review.
They should not be considered conclusive, used to inform clinical practice,
or referenced by the media as validated information.

Study on lithium battery heat dissipation based on a fence structure of liquid cooling and phase change optimization

Youliang Chen
Wuhan University of Science and Technology
Bo Zhao
zhaobo87@wust.edu.cn
Wuhan University of Science and Technology
Fengye Li
Wuhan University of Science and Technology

Research Article

Keywords: Battery thermal management, Fence structure, Counter-flow coolant, Phase change materials, Temperature uniformity

Posted Date: July 14th, 2026

DOI: https://doi.org/10.21203/rs.3.rs-9877472/v1

License: This work is licensed under a Creative Commons Attribution 4.0 International License.
Read Full License

Additional Declarations: No competing interests reported.

Study on lithium battery heat dissipation based on a fence structure of liquid cooling and phase change optimization

Youliang Chen[1], Bo Zhao[1,2*], Fengye Li[2]

1 Hubei Key Laboratory for Efficient Utilization and Agglomeration of Metallurgic Mineral Resources, Wuhan University of Science and Technology, Wuhan, 430081, P.R. China

2 Industrial Safety Engineering Technology Research Center of Hubei Province, Wuhan University of Science and Technology, Wuhan, 430081, P.R. China

Abstract

In conventional horizontal cold plates, the internal heat generated by the battery pack cannot be effectively dissipated. The temperature inside the battery pack is significantly higher than that of the surrounding areas. To address the significant temperature gradient between the central and peripheral regions of the battery pack, the heat dissipation method of phase change material-fence liquid cooling was used to analyze the influence of fence structure, the parallel counter flow coolant arrangements, and the wrapping method of phase change material on the battery heat dissipation. The results showed that the parallel-counter flow of coolant can avoid the temperature increase of the battery with the flow direction. The battery cooling method with the parallel-counter flow coolant arrangements and fence structure reduces the maximum temperature from 328.91 K to 315.86 K compared to the Parallel flow cooling arrangement. The temperature difference is decreased from 6.47 K to 5.78 K, improving the uniformity of the temperature distribution. In addition, the temperature uniformity of the battery

module can be improved by adopting a scheme where phase change material is wrapped around it, reducing the temperature difference from 5.78 K to 4.12 K.

Keywords

Battery thermal management; Fence structure; Counter-flow coolant; Phase change materials; Temperature uniformity

Nomenclature variables

I	operating current (A)	α_c	the transfer coefficients of the cathode
V_{oc}	open-circuit voltage (V)	η	Overpotential (V)
V	operating Voltage (V)	ρ_s	Density (kg/m^3)
j	Current density (A/m^2)	v	kinematic viscosity of water (m^2/s)
i_0	exchange current (A)	θ	thermal conductivity of PCM (w/m×K)
L	electrode thickness (m)	β	the coefficient of thermal expansion of the fluid (1/K)
F	faraday constant (96485 C/mol)	**Subscripts**	
R	general gas constant (8.314 J/mol×K)	l	liquid
C_p	specific heat capacity at constant pressure (J/kg×k)	s	solid

K_s	thermal conductivity of battery (w/m×K)	*matrix*	porous medium
$\vec{v}$	flow velocity (m/s)	*eff*	effective
p	Pressure (pa)	**Acronyms**	
H	Enthalpy	LIB	lithium battery
T	Temperature (K)	PCM	phase change material
f_l	Liquid phase fraction	NCM	lithium nickel cobalt manganese oxide
L	latent heat of phase transition (J/kg)	LFP	lithium iron phosphate
Greek symbols		NTGK	Newman, Tiedemann Gu and Kim
α_a	the transfer coefficients of the anode	ECM	equivalent circuit model

1 Introduction

Compared with other batteries, lithium batteries have the advantages of high energy density, long service life and high cycle time[1,2]. Lithium batteries account for more than 80% of the utilization of power batteries in automobiles. However, the performance and lifespan of lithium batteries are closely tied to the battery's operating temperature[3-5]. When the temperature is too high or too low[6,7], it will accelerate the battery life decline. Furthermore, power batteries are being designed to be larger and larger. This makes it harder for internal heat to dissipate, leading to more issues, such as uneven temperature distribution and rapid local heating. If the battery continues to operate with excessive temperature differences persisting over time, it will seriously

affect the battery's cycle life and performance[8-11].

Currently, based on the variations in battery packs and cooling media, the cooling systems for power battery modules are primarily categorized into three types: air cooling, liquid cooling, and PCM-based cooling systems. Although air cooling is safe and simple, the heat capacity and thermal conductivity of air are much lower than many other mediums, thus air-based systems still face issues with temperature rise and uneven temperature distribution among cells[12-14]. In PCM-based cooling, phase change materials with a large specific heat capacity can alter their physical state, a process that absorbs a large amount of heat[15-17]. Using phase change materials to cool batteries is highly energy efficient and well suited to various shapes of batteries. However, phase change materials can only help control the temperature of the battery when they are not completely melted[18,19]. The current use of a single phase change material cannot be adapted to the complex environment of power batteries due to large-scale and high discharge rates, it may melt into liquid after absorbing heat, leading to a more complex and dangerous battery pack structure, or even destroy the battery pack structure[20-22].

In liquid cooling, which is more efficient due to higher heat transfer coefficient of water[23,24]. Liu et al.[25] found that liquid cooling was generally more effective in temperature reducing compared to phase-change material, while the latter can lead to more homogeneous temperature distribution. Therefore, coupling liquid cooling with PCM cooling can leverage the respective advantages of both thermal management methods[26-28]. Zhang et al.[29] experimentally investigated a large-sized power battery

module by PCM and bottom liquid cooling techniques, finding that compared with a single cooling method, the hybrid cooling reduced the maximum battery temperature and temperature difference. However, this structure can cause temperature accumulation in the middle part of the battery pack, resulting in uneven temperature distribution. Bai et al.[30]designed a hybrid cooling methods, that liquid cooling is used in the upper part and phase change material is placed in the lower part between the two battery cells. This structure can timely take away the heat in the middle of the battery pack and reduce the temperature difference, but the temperature distribution around the battery pack is uneven. At 3 C discharge rate, Ping et al.[31] proposed a novel phase change material-liquid-phase tube coupled thermal management method, suggesting that the maximum temperature and temperature difference of the battery pack were 47.6 ℃ and 4.5 ℃, respectively. Gao et al.[32] proposed a novel battery thermal management system that combines composite phase change materials with dual S-shaped microchannel liquid cooling technology, to enhance the thermal conductivity of the phase change materials, they added expanded graphite (EG) to paraffin, the maximum temperature and the maximum temperature difference were 41 ℃ and 5.9 ℃, respectively. Zhuang et al.[33] proposed a hybrid battery thermal management system (BTMS) that combines phase-change materials (PCM) arranged in a honeycomb pattern with cooling plates, wax and ethylene glycol are used as the PCM and coolant respectively, the maximum temperature is 48.5 ℃ and the maximum temperature difference is 6.3 ℃.

Most of the aforementioned studies have integrated horizontal cold plates with phase change materials (PCMs). However, this traditional planar contact method is often constrained by a restricted heat exchange area. Under high-rate battery discharge or complex operating conditions, it is prone to issues such as localized overheating and uneven temperature distribution within the battery pack, thereby limiting the overall efficiency of the thermal management system. To overcome the heat transfer bottlenecks of traditional horizontal cooling structures, this research proposes an innovative multi-dimensional battery thermal management system. This system features a uniquely designed fence-structured cold plate, a parallel-counter flow coolant configuration, and a PCMs wrapping technique. Numerical simulations were conducted using ANSYS to analyze the effects of the discharge rate, cold plate configuration, coolant inlet velocity, and PCM thickness. Furthermore, rather than relying solely on macroscopic indicators like maximum temperature and temperature differences, this study investigates the underlying mechanisms by calculating the heat flux of individual cells and conducting a variance analysis.

2 Model

2.1 Physical problem

As shown in Fig. 1a, the hybrid cooling method incorporates the fence structure, the water flows in opposite directions and the wrapping method of phase change material. The battery pack consists of five individual cells configured in the arrangement illustrated in Fig. 1b. The fence structure is composed of horizontal cold plate and

vertical cold plate, as shown in Fig. 1c. The symmetric serpentine channel is selected as the flow path, compared with the serpentine channel, it has little pressure difference and low energy consumption[34,35]. Meanwhile, the structural design of the symmetric serpentine channel is more effective in controlling the maximum temperature and the overall temperature difference of the model. The horizontal cold plate is shown in Fig. 1d, with a size of 148×98×4 mm.

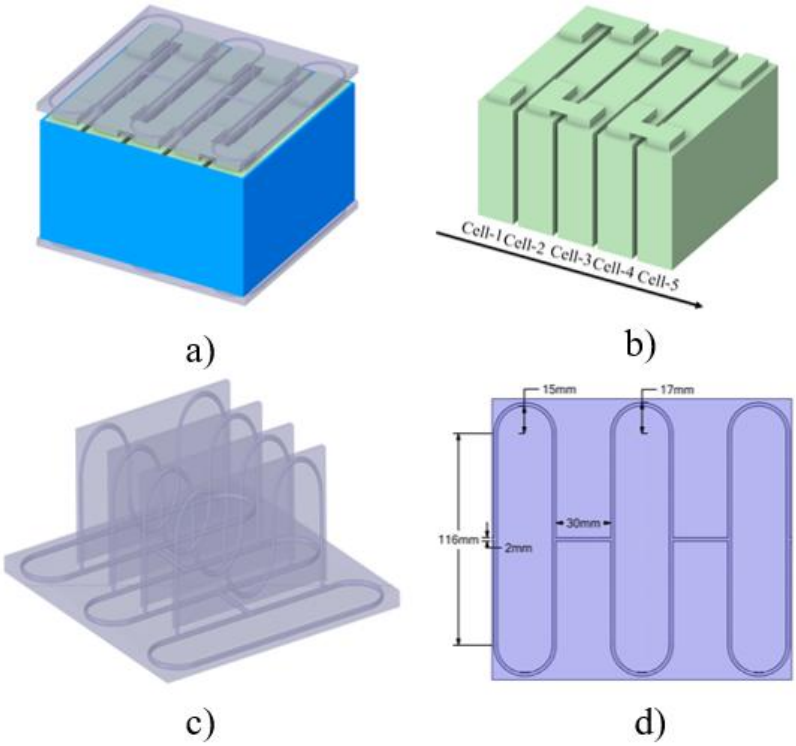


Fig.1 a) Schematic of the hybrid cooling method with liquid cooling and PCM cooling b) Physical Layout of the Battery Pack c) Schematic of the fence structure d) The horizontal cold plate

In the case of cold plate cooling applied above and below the battery, the four lateral surfaces of the battery pack can be effectively cooled by using composite phase change materials, thereby enhancing temperature distribution uniformity. In this study, to

enhance the thermal conductivity of the phase change material[36,37], a copper foam - paraffin composite phase change material was adopted. The thermal conductivity, latent heat, and specific heat capacity of these materials vary with porosity. By calculating the properties at different porosity levels, the corresponding thermal parameters are determined.

Table 1 Specific heat capacity and thermal conductivity at different porosity rates

Porosity (%)	**Mass fraction of copper foam (%)**	**Specific heat capacity of composite phase change materials （J/kg×K）**	**Thermal conductivity （W/m×K)**	**Equivalent specific heat capacity of composite phase change materials （J/kg×K）**
70	82	3256	119.8	634
80	66	2039	79.9	761
90	55	1633	40.4	1015
100	0	822	0.156	1770

(The equivalent specific heat capacity of a composite phase change material is the specific heat capacity of the composite phase change material with respect to time when the phase change occurs.)

As listed in Table 1, the composite phase change material (CPCM) employed in this study features copper foam with a porosity of 90%, because the percentage of copper foam in this material was relatively small (cost savings), but the material has a high

specific heat capacity, thermal conductivity and equivalent specific heat capacity.

2.2 Battery model

Currently, the batteries predominantly utilized in electric vehicles are lithium nickel cobalt manganese oxide ($LiNi_xCo_yMn_zO_2$, NCM) and lithium iron phosphate ($LiFePO_4$, LFP) batteries[38,39]. Huang et al.[40] conducted a comparative analysis of the thermal runaway (TR) propagation behavior in NCM and LFP modules. Although NCM LIB exhibits a higher energy density[41], the duration of thermal runaway and the peak temperature are significantly higher compared to those of LFP LIB. The battery pack module consists of 5 single batteries connected in series and the single NCM LIB parameters are shown in Table 2.

Table 2 NCM LIB parameters

parameters	value	parameters	value
Battery length, width and height /mm	148*28*92	**Positive Length Width Height/mm**	38*18*6
Negative Length, Width and Height /mm	22*18*6	**Nominal capacity /Ah**	40
Operating voltage /V	3.65	**Weight/Kg**	0.83

The electrochemical model of a battery is very complex. Generally, the Bernadine

equation is used to calculate the heat generation of the battery, which consists of two parts: Joule heat and reaction heat.

$$q=I\cdot(V_{oc}-V)-I\cdot T\cdot\frac{\partial V_{oc}}{\partial_T} \quad (1)$$

Where q is volumetric heat generation rate, I is operating current, V_{oc} is open-circuit voltage, V is operating Voltage, T is absolute temperature, $\frac{\partial V_{oc}}{\partial_T}$ is entropy heat coefficient.

In this work, the NTGK model in fluent software is adopted to calculate the heat generation of the battery, which correlates the current with the overpotential of the battery through an analytical expression:

$$j=\frac{i_0}{L}\left[EXP\left(\frac{\alpha_a F}{RT}\eta\right)-EXP\left(-\frac{\alpha_c F}{RT}\eta\right)\right] \quad (2)$$

Where j, i_0, L, α_a, α_c, F, R, T and η represents the current density, exchange current, electrode thickness, the transfer coefficients of the anode and cathode, faraday constant, general gas constant, temperature and overpotential, respectively. The NTGK model can simultaneously calculate the Joule effect and reaction heat of the battery. Compared with the ECM model which only calculates the Joule heat, the heat generation rate is more accurate.

2.3 Governing equations

For the square lithium batteries, which is regarded as porous media or solids, and the energy conservation equation is as follows:

$$\rho_s C_{pm,s}\frac{\partial T}{\partial t}=\nabla\cdot(K_s\nabla T)+q \quad (3)$$

Where ρ_s, $C_{pm,s}$ and K_s are the density, specific heat capacity at constant pressure

158 and thermal conductivity of battery.

159 The water was selected as the cooling medium in the LIB module. The energy
160 conservation equation of liquid water within the cooling-plate is as follows:

161 $$\frac{\partial T}{\partial t}+(\vec{v}\cdot\nabla)T=\alpha\nabla^2 T \tag{4}$$

162 Where $\vec{v}$ is cross-sectional average flow velocity and α is thermal diffusivity.

163 The continuity equation of cooling water is shown in equation (5):

164 $$\nabla\cdot\vec{v}=0 \tag{5}$$

165 The momentum conservation equation of cooling water is given as follows:

166 $$\frac{\partial\vec{v}}{\partial t}+(\vec{v}\cdot\nabla)\vec{v}=-\frac{1}{\rho}\nabla p+\nu\nabla^2\vec{v} \tag{6}$$

167 Where ρ and ν is the density and kinematic viscosity of water, ∇p is the pressure
168 drop.

169 PCM absorbs heat and undergoes a phase change, the energy conservation equation
170 in PCM can be seen as the following equation:

171 $$\rho\frac{\partial H}{\partial t}=\theta\left(\frac{\partial^2 H}{\partial x^2}+\frac{\partial^2 H}{\partial y^2}+\frac{\partial^2 H}{\partial z^2}\right) \tag{7}$$

172 where ρ, H and θ are the density, enthalpy and thermal conductivity of PCM.

173 To consider the natural convection effect of PCM materials, the Boussinesq
174 approximation is applied, which only considers the density change in the term related
175 to volume force (gravity). While treating density as a constant in all other parts of the
176 control equation, it results in a buoyancy source term. The equation is as follows:

177 The density change is very small and can be expressed as:

178 $$\rho=\rho_0[1-\beta(T-T_0)] \tag{8}$$

Where ρ is the actual density, ρ_0 is the reference density at the reference temperature T_0, β is the coefficient of thermal expansion of the fluid.

Simplify the momentum equation in the y-direction to:

$$\rho_0\left(u\frac{\partial_v}{\partial_x}+v\frac{\partial_v}{\partial_y}\right)=-\frac{\partial_p}{\partial_y}+\mu\left(\frac{\partial^2{}_v}{\partial_{x^2}}+\frac{\partial^2{}_v}{\partial_{y^2}}\right)+\rho g \tag{9}$$

Usually, the pressure p is decomposed into hydrostatic pressure and dynamic pressure，$p=p_{\mathrm{h}}+p_d$, and $\frac{\partial_{p_{\mathrm{h}}}}{\partial_y}=-\rho_0 g$. The final expression is given in Equation (10):

$$\rho_0\left(u\frac{\partial_v}{\partial_x}+v\frac{\partial_v}{\partial_y}\right)=-\frac{\partial_{p_d}}{\partial_y}+\mu\left(\frac{\partial^2{}_v}{\partial_{x^2}}+\frac{\partial^2{}_v}{\partial_{y^2}}\right)-\rho_0 g[1-\beta(T-T_0)] \tag{10}$$

Among them, $-\rho_0 g[1-\beta(T-T_0)]$ directly reflects the buoyancy effect driven by temperature difference.

The foam metal material is filled into the PCM material. The composite phase change material (CPCM) combines the dual advantages of PCM's high heat storage density and foam copper's high thermal conductivity.

To consider the flow and melting process of PCM material in a porous medium (foam metal), the following assumptions are made: 1) The porous medium is rigid, uniform and isotropic. 2) PCM is incompressible both in solid and liquid states. 3) The flow of liquid-phase PCM is laminar. 4) Considering natural convection, the Boussinesq approximation is adopted. 5) Use the assumption of local thermal equilibrium[42].

The governing equations are as follows.

$$\left(\rho C_p\right)_{eff}\frac{\partial T}{\partial t}+\left(\rho C_p\right)_l v\cdot\nabla T=\nabla\cdot\left(k_{eff}\nabla T\right)-\rho_l L\frac{\partial f_l}{\partial t} \tag{11}$$

Where v is the Darcy velocity of liquid PCM, L is the latent heat of phase

transition of PCM, f_l is the liquid phase fraction, $(\rho C_p)_{eff}$ is the effective volumetric heat capacity, the equation is listed as follow:

$$(\rho C_p)_{eff}=\phi[f_l\rho_l C_{p,l}+(1-f_l)\rho_s C_{p,s}]+(1-\phi)\rho_{matrix}C_{p,matrix} \quad (12)$$

$$f_l=\begin{cases}0 & T<T_s \\ \dfrac{T-T_s}{T_l-T_s} & T_s\leq T\leq T_l \\ 1 & T>T_l\end{cases} \quad (13)$$

Where ϕ is the porosity of porous media, C_p represents specific heat capacity at constant pressure, the subscripts l, s and $matrix$ respectively represent liquid PCM, solid PCM and porous medium.

The heat generated within the battery is conducted to its surface and subsequently dissipated by a cooling medium (e.g., air or liquid coolant). At the solid-fluid interface, the heat flux balance is governed by the following equation:

$$-k\frac{\partial T}{\partial n}=h(T_s-T_f) \quad (14)$$

Where $-k\frac{\partial T}{\partial n}$ is heat flux, h is the convective heat transfer coefficient of the cooling system, T_s is the battery surface temperature, T_f is the temperature of the cooling medium.

2.4 Numerical method and validation

For the battery pack, to simulate the natural convection of the battery pack under the vehicle, it is set that there is natural convection between the surface of the battery pack and the environment, with a convection coefficient of 5 $w/k\times m^2$. For the liquid cooling area of the battery pack, the cold plate is made of aluminum, and water is selected as the coolant. The flow of the coolant adopts the Realizable wall function, and both the

speed inlet and pressure outlet are used. For the PCM cooling region, due to the use of the Boussinesq approximation, the overall model needs to be calculated under a gravitational acceleration of $9.8\ m^2/s$.

Transient simulations of the liquid and phase-change cooling systems were performed using the pressure-based transient solver in ANSYS Fluent, accounting for the natural convection of the phase-change material (PCM) and the non-uniform heat generation of the battery. To accurately capture the phase transition phenomenon, the energy equation was solved in conjunction with the solidification/melting model. Furthermore, the SIMPLE algorithm was employed for pressure-velocity coupling, and a second-order upwind scheme was utilized to discretize both the momentum and energy equations, thereby enhancing the overall accuracy of the solution.

In the simulation, the model is divided into different mesh numbers, and the relationship between the maximum temperature and the mesh number is calculated as shown in Fig. S1.

In Fig. S1, when the mesh number increases from 1591335 to 3992975, the maximum temperature change range is within 0.08%. If the number of grids continue to increase, the difference between the results is small, proving the grid independence of the model.

To verify the accuracy of the lithium battery thermal behavior model, the simulation results are compared with the experimental data of the maximum temperature at different discharge rates in ref. 41[43], the model uses the same boundary and

thermophysical parameters as those in the experiments[43]. The comparison results are shown in Fig. S2. At different discharge rates, the maximum deviation between the maximum temperature data of the battery pack experiment and the numerical simulation does not exceed 1k. The good consistency confirmed the accuracy of the battery heating model in this study.

For the verification of the PCM cooling model, a 2D model of 100 × 100mm was established for paraffin and copper foam-paraffin composite phase change materials (copper foam with a porosity of 98%), respectively. The left side is set as the heating wall with a heat flux of 1200 w/m^2, while the other three sides are adiabatic non-sliding walls. The simulation results are shown in Fig. S3. Under the same boundary conditions, The liquid fraction distribution of the phase-change material during melting, obtained through numerical simulation, showed good agreement with the experimental results reported by Zheng et al.[44], under the same boundary conditions, due to the influence of natural convection, the melting speed of the upper part of both materials is faster than that of the lower part. However, the copper foam in the composite material can increase the thermal conductivity of the phase change material, making the temperature distribution of the composite phase change material more uniform than that of the single phase. Composite materials are more suitable for cooling battery packs.

3 Results and Discussion

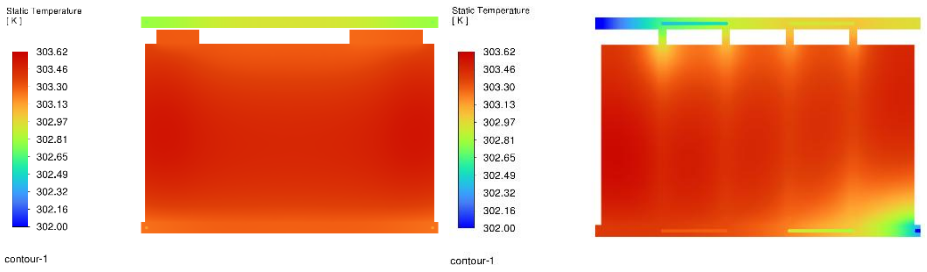
3.1 Hybrid cooling arrangement at different discharge rates

The battery pack is operated in a hybrid cooling arrangement. The ambient

261 temperature is 300 K, and the water flow rate is set as 0.1 m/s. The temperature cloud
262 at different discharge rates with the hybrid cooling arrangement are shown in Fig. S4.
263 At different discharge rates, the lowest temperature of the battery pack is located at the
264 water inlet of the lower cold plate. Moreover, as the discharge rate increases, the
265 temperature stratification at the water inlet of the lower cold plate becomes obviously.
266 Fig. 2 is the temperature cloud of the symmetry axis section of the battery pack，
267 indicating that the temperature distribution of the batteries in the middle of the battery
268 pack is very uniform. The temperature stratification mainly occurs on the first battery
269 close to the water inlet of the lower cold plate, while the temperature distribution of the
270 other batteries is relatively uniform. It is attributed to the setting arrangement of the
271 cold plate and the PCM around.

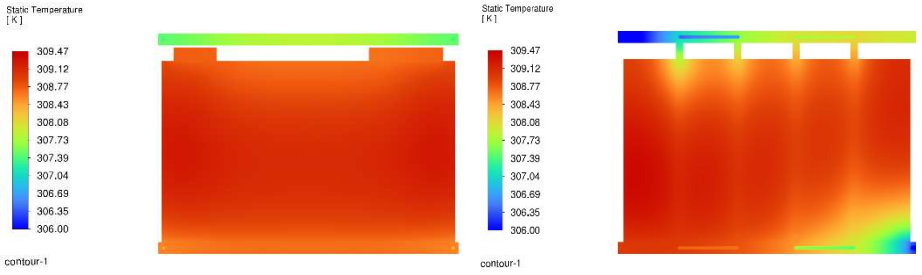
272 X direction: Y direction:

273 1C:



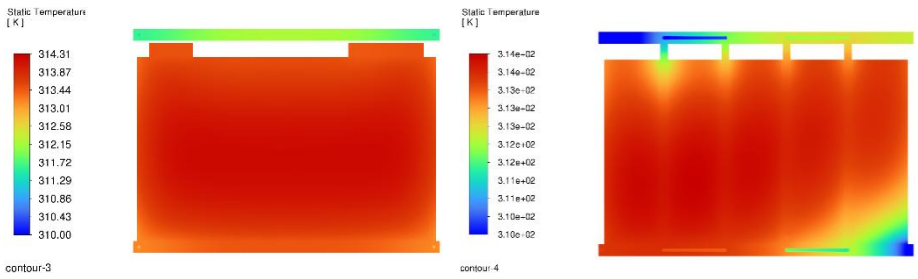
274

275 2C:



276

3C:



4C:

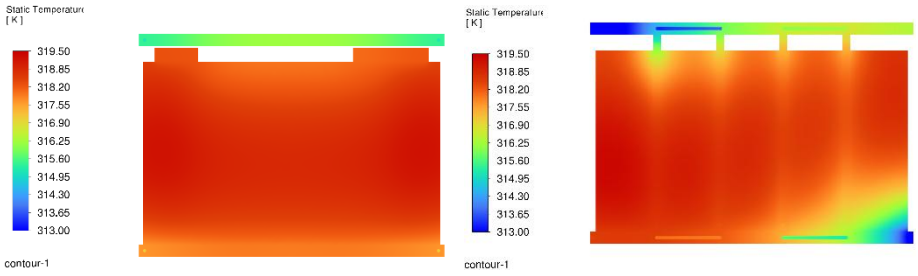
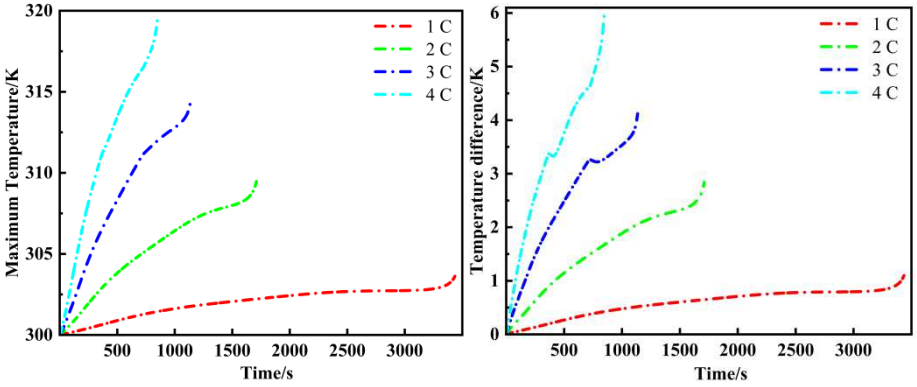


Fig. 2 Temperature cloud of the symmetry axes (x, y) of battery packs at different discharge rates

Subsequently, the maximum temperature and temperature difference are extracted to provide a quantitative assessment of the thermal performance. Fig. 3 showed the maximum temperature and temperature difference of the battery pack at different discharge rates in the hybrid cooling arrangement. As the discharge increased from 1 C to 4 C, the maximum temperatures were 303.62 K, 309.47 K, 314.31 K and 319.51 K, respectively, with maximum temperature differences of 1.1 K, 2.84 K, 4.12 K and 6.05 K, respectively. It can further be observed from Fig. 6 that, at discharge rates of 3 C and 4 C, the temperature-difference curve exhibits a temporary dip, indicating a slowed growth trend, whereas no such inflection appears at 1 C and 2 C. This phenomenon is closely associated with the melting behavior of the PCM, which absorbs a considerable

amount of latent heat once its melting temperature is reached.



Maximum temperature Temperature difference

Fig. 3 The maximum temperature and temperature difference of the hybrid cooling method at different discharge rates

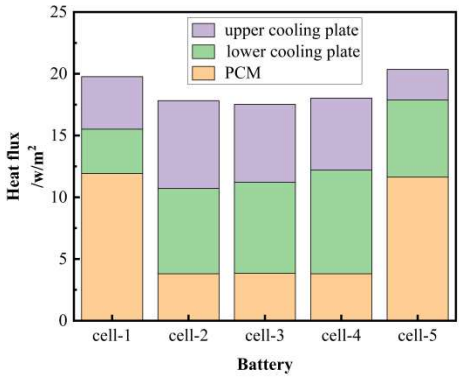


Fig. 4 Heat flux under hybrid cooling conditions at a discharge rate of 3 C

To further elucidate the underlying mechanism, the liquid fraction (LF) contours of the PCM at discharge rates of 3 C and 4 C are shown in Fig. S5. At lower discharge rates (1 C and 2 C), the heat generation is insufficient to initiate substantial phase transition, so the PCM dissipates heat primarily through sensible heat, and no inflection is observed in the temperature-difference curve. In contrast, at 3 C and 4 C, the PCM undergoes significant melting, and the latent heat absorption effectively suppresses the

306 temperature rise, which explains the inflection observed in the ΔT curves. This confirms
307 the critical role of the PCM in stabilizing the thermal response of the battery pack under
308 high-rate discharge.

309 To further investigate the contribution of each cooling pathway, Fig. 4 presents the
310 heat flux composition of the five battery cells at a discharge rate of 3 C, decomposed
311 into three cooling routes: the upper cold plate, the lower cold plate, and the PCM.
312 Overall, Cell-1 and Cell-5 (the edge cells) exhibit the highest total heat flux, reaching
313 approximately 20 W/m², while the middle cells (Cell-2, Cell-3, and Cell-4) show
314 slightly lower values in the range of 17–18 W/m². In terms of the cooling pathway
315 distribution: 1) Edge cells (Cell-1 and Cell-5) rely predominantly on the PCM, which
316 accounts for more than half of their total heat dissipation (approximately 11–12 W/m²).
317 2) Middle cells (Cell-2, Cell-3, Cell-4) show a much smaller PCM contribution (less
318 than 5 W/m²) but dissipate significantly more heat through the lower cold plate
319 (approximately 7–8 W/m²). 3) The contribution of the upper cold plate remains
320 relatively uniform across all cells, ranging between 4 and 7 W/m², with slightly higher
321 values for Cell-2 and Cell-3.

322 In summary, Fig. 4 clearly reveals a spatially dependent cooling mechanism: edge
323 cells dissipate heat mainly through the surrounding PCM, whereas middle cells rely
324 more heavily on the lower cold plate. This complementary cooperation between the
325 PCM and the liquid cold plates ensures balanced heat removal across the entire battery
326 pack and underpins the excellent temperature uniformity observed in the preceding

327 analysis.

328 ***3.2 Effect of cold plate arrangement***

329 The cold plate is important for heat removing from the battery pack. The arrangement
330 of the cold plate has a significant impact on the maximum temperature and temperature
331 difference of the battery pack. In this section, four cases with different arrangement
332 were considered and simulated. The inlet mass flow velocity is 0.1m/s, the shapes of
333 the cold plate channels are all symmetrical serpentine and the pipe diameters are 2 mm.
334 In the four cases, the arrangements of the cold plate are different, but all without PCM
335 added, as shown in Fig. S6. The four cases differ only in the cold-plate arrangement:

336 Case 1: a conventional single cold plate placed beneath the battery pack;

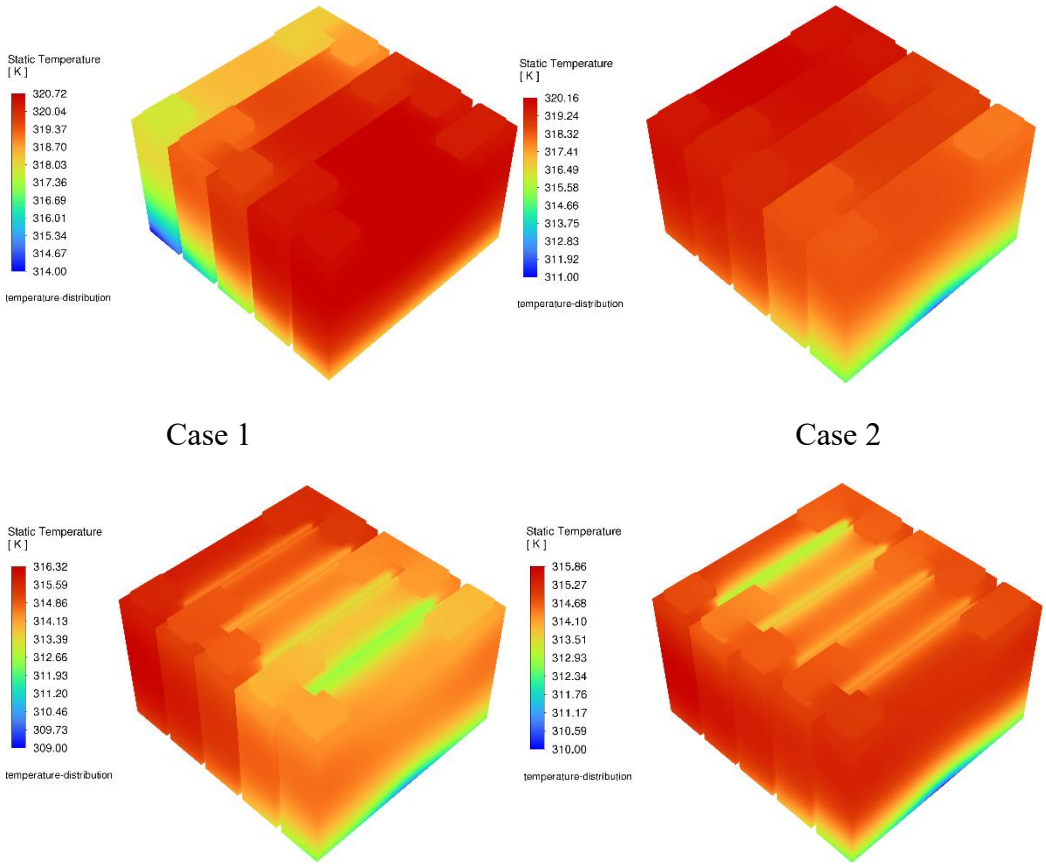
337 Case 2: a single cold plate beneath the battery pack with an added fence structure;

338 Case 3: two cold plates with fence structure arranged on the top and bottom of the
339 battery pack, with adopting parallel flow;

340 Case 4: two cold plates with fence structure arranged on the top and bottom of the
341 battery pack, with counter-current flow.

342 Fig. 5 shows the temperature contours of the battery pack under the four cases,
343 providing a direct view of the spatial temperature field. Comparing Case 1 with Case 2,
344 the fence structure visibly shrinks the local high-temperature region on the cell surface,
345 indicating an enhancement of the local heat-extraction capability. From Case 2 to Case
346 3, the introduction of an additional cold plate on the opposite face of the battery pack
347 eliminates the strong temperature gradient in the thickness direction and produces a

markedly more uniform field. Case 4 further smooths the streamwise temperature gradient: the counter-current arrangement of the upper and lower cold plates compensates for the coolant enthalpy rise along the flow path, so that no pronounced hot zone can be identified near the outlet.



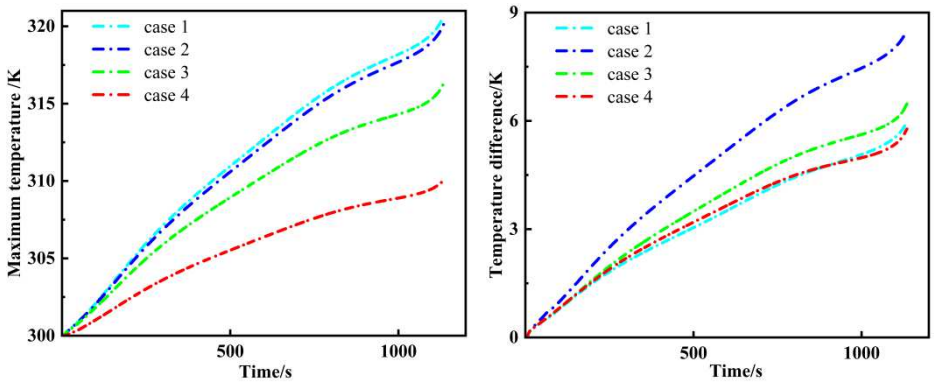
Case 1 Case 2

Case 3 Case 4

Fig. 5 Temperature cloud diagrams of battery with different setting arrangement (case 1, case 2, case 3, case 4) at 3 C.

Fig. 6 was the maximum temperature（T_{Max}) and the maximum temperature difference (ΔT_{Max}) under the four cases at 3 C discharge rate. From case 1 to case 4, the maximum temperatures were 320.72 K, 320.16 K, 316.33 K, and 315.86 K, respectively, with maximum temperature differences of 5.99 K, 8.2 K, 6.47 K and 5.78

K, respectively. A counter-intuitive result is observed between Case 1 and Case 2: the fence structure lowers T_{Max} by only 0.56 K, yet raises ΔT_{Max} by 2.21 K. The fence enhances local convective heat extraction and pulls down the minimum temperature of the cell surface, but this localized enhancement simultaneously enlarges the spread of cell-surface temperatures and thus degrades the overall temperature uniformity. From Case 2 to Case 3, adding a second cold plate on the upper surface of the battery pack reduces T_{Max} by 3.83 K and ΔT_{Max} by 1.73 K, demonstrating that increasing the number of cooling surfaces substantially improves the overall cooling performance. From Case 3 to Case 4, switching from parallel to counter-current flow further reduces T_{Max} by 0.47 K and ΔT_{Max} by 0.69 K, because the counter-current arrangement balances the heat-removal capacity between the inlet and outlet ends and suppresses the streamwise temperature rise.



Maximum temperature Temperature difference

Fig. 6 Maximum temperature of the battery under different setting arrangement and temperature difference of battery with different setting arrangement (Case 1, Case 2, Case 3, Case 4) at 3 C.

To uncover the heat-transfer mechanism underlying the temperature behavior above,

the cell-surface heat-flux distributions of the four cases are compared in Fig. 7. The variance of the heat flux, $\sigma^2(q)$, is adopted as a quantitative indicator of heat-dissipation uniformity at the module level: a smaller $\sigma^2(q)$ corresponds to more consistent heat extraction across the five cells, whereas a larger value implies pronounced cell-to-cell disparity. Comparing Case 1 and Case 2, $\sigma^2(q)$ drops from 1.9724 to 0.9368, a reduction of about 52.5%. This shows that the fence structure not only enhances the local heat-transfer coefficient but also redistributes the heat flux more evenly among the cells. The effect of flow direction is examined by comparing Case 3 and Case 4. $\sigma^2(q)$ decreases from 1.8417 under parallel flow to 1.2789 under counter-current flow. As shown in Fig. 7, Case 4 exhibits a flat heat-flux profile across the five cells, whereas Case 3 shows pronounced fluctuations with a clear disparity between the cells near the inlet/outlet and those in the middle. This is fully consistent with classical heat-exchanger theory: under a counter-current arrangement the local driving temperature difference between coolant and cell remains nearly constant along the channel, producing a uniform local heat flux; under parallel flow, the driving temperature difference decays along the channel, leading to uneven heat extraction. Combining the fence structure with the counter-current flow strategy is therefore an effective route to reducing $\sigma^2(q)$ and enhancing thermal consistency at the module level.

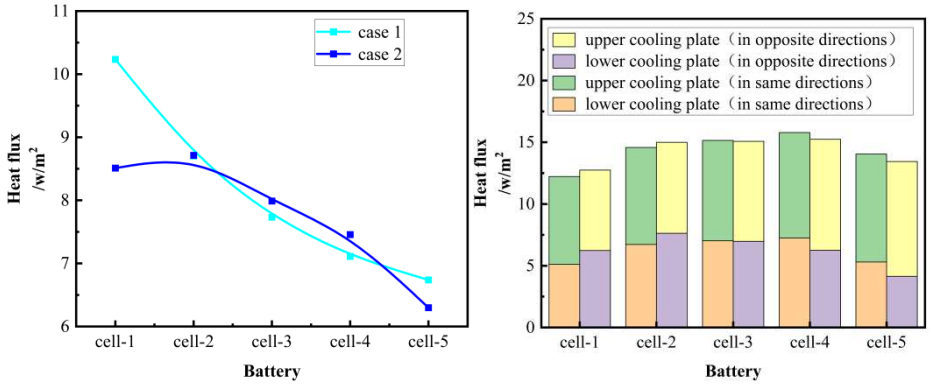


Fig. 7 Heat flux of the battery under different arrangement (case 1, case 2, case 3, case 4) at 3 C.

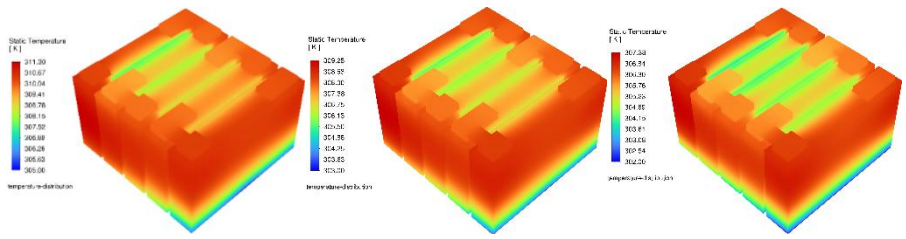
Notably, in Case 2, the enhancement in heat flux uniformity is accompanied by an increase in ΔT_{Max}. It indicates that enhancing local heat transfer uniformity does not guarantee a uniform temperature distribution.

This divergence aligns with classical heat exchanger theory[44], which establishes that thermal and heat transfer coefficient maldistributions are conceptually independent yet coupled. Although Case 2 homogenizes the local heat flux, the coolant's continuous sensible heat absorption along the flow path leads to a substantial temperature rise, which often dominates the overall ΔT_{Max} in battery cooling[45]. Similar trade-offs are frequently reported in related fields. Studies by Deng et al.[46] found that improving the local Nusselt number (Nu) distribution via channel modifications ironically increased the module's ΔT_{Max} due to flow redistribution. Chein and Chen[47] found that certain inlet/outlet arrangements in microchannel heat sinks yield a more uniform h field but a larger substrate ΔT_{Max}. These results collectively confirm that the non-monotonic coupling between $\sigma^2(q)$ and ΔT_{Max} is a generic feature of liquid-cooled systems, not an isolated artifact of the present geometry.

3.3 Effect of the water flow velocity

The water flow velocity is an important factor affecting the cooling performance of the cold plate when using liquid cooling. In this section, four inlet velocities ranging from 0.1 m/s to 1 m/s were selected to study their influence on the cooling performance of cold plates at 3 C discharge rate.

The temperature distribution of battery under different flow velocity at the end of the discharging was shown in Fig. 8. The temperature distribution difference of the battery pack becomes increasingly large with the increase of water flow velocity. Meanwhile, the lowest temperature of the battery pack is in the water flow inlet area, the highest temperature occurs at the battery pack electrodes, and color stratification appears at the bottom and top of the battery pack.

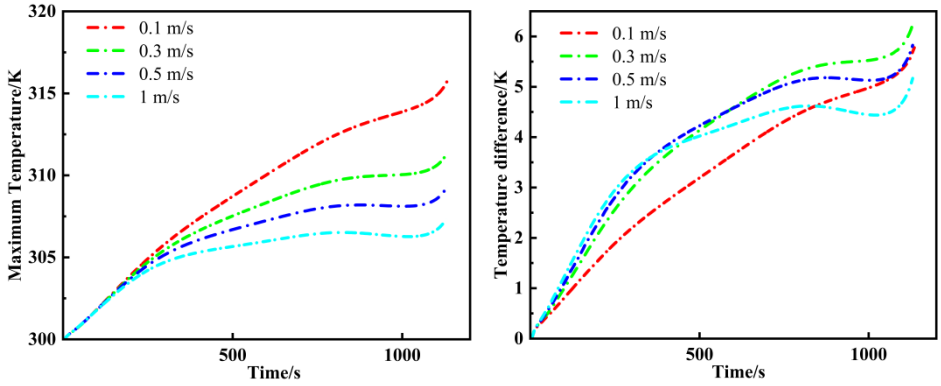


V=0.3*m*/*s* *v*=0.5*m*/*s* *v*=1*m*/*s*

Fig. 8 Temperature distribution of battery under different flow velocity

The maximum temperature and temperature difference is shown in Fig. 9, as the water flow velocity increased from 0.3 m/s to 1 m/s, the maximum temperatures were 311.3 K, 309.25 K and 307.38 K, respectively, with maximum temperature differences of 6.23 K, 5.82 K and 5.17 K, respectively. By comparing the maximum temperature, it can be found that as the water velocity increases, the maximum temperature

continuously decreases, but the extent of the decrease becomes smaller and smaller. By observing the temperature difference curve, from the start of discharge to 500 seconds, the maximum temperature difference increases with the increase of water flow velocity. However, in Fig. 9, the maximum temperature difference at water velocities of 0.5 m/s and 1 m/s is lower than that at 0.1 m/s. It is because that at a higher water flow rate, the maximum temperature of the battery pack is close to the ambient temperature and water temperature.



Maximum temperature Temperature difference

Fig. 9 The maximum temperature and temperature difference of the battery under different flow velocity

Pressure drops under different flow velocity are shown in Table 3 and Fig. S7. The water flow velocity increased from 0.1 m/s to 1 m/s, and the pressure drop rose from 196 pa to 4086 pa. As the water velocity increased, the pressure drop rose rapidly.

From the above analysis, it can be seen that a higher water flow rate can reduce the maximum temperature of the battery pack. However, as the water flow rate increases, it intensifies the uneven temperature distribution of the battery pack, and the pressure drop increases rapidly, consuming a large amount of energy. Therefore, when choosing

454 the water flow velocity, the relationship among the maximum temperature, temperature
455 distribution and pressure drop should be taken into consideration. In this study, it is
456 more appropriate to choose the water velocity of 0.1 m/s.

457 Table 3 Pressure drop under different flow velocity.

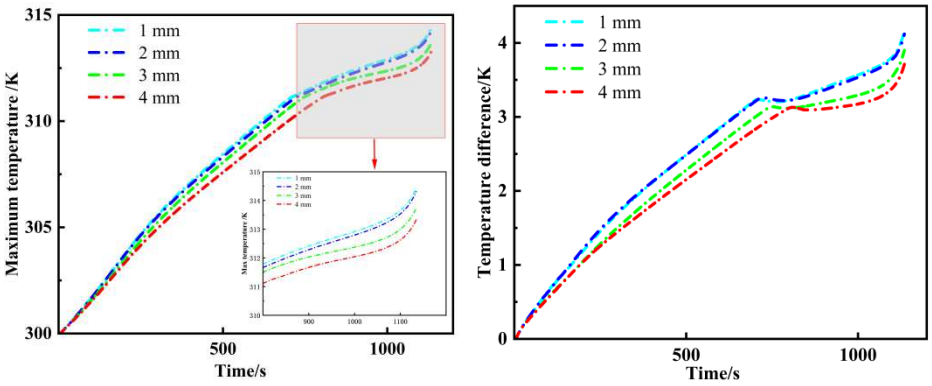
Flow velocity (m/s)	0.1	0.3	0.5	1
Pressure drop (pa)	196.4599	773.4367	1558.94	4086.132

458 ***3.4 Effect of the PCM thickness***

459 The arrangement of the cold plate takes away most of the heat from the battery pack.
460 Due to the different heat transfer coefficients of the cooling medium, there is still a
461 temperature difference in the area around the battery pack that comes into contact with
462 the cold plate. To further reduce the temperature difference, the PCM is around the
463 battery pack. This section examines the effect of PCM thickness on the hybrid cooling
464 system performance at a water velocity of 0.1 m/s and 3C discharge rate. When the
465 thickness of the PCM changes from 1 mm to 4 mm, the maximum temperature and
466 temperature difference are shown in the Fig. 10.

467 As the thickness of the PCM increased from 1 mm to 4 mm, the maximum
468 temperatures were 314.43 K, 314.31 K, 313.73 K, and 313.32 K, respectively, with
469 maximum temperature differences of 4.16 K, 4.12 K, 3.9 K, and 3.71 K, respectively.
470 As the thickness of the PCM increases, both the maximum temperature and the
471 temperature difference of the battery pack decrease. From 1 mm to 4 mm, the maximum
472 temperature drops by 1.1 K and the maximum temperature difference decreases by 0.5

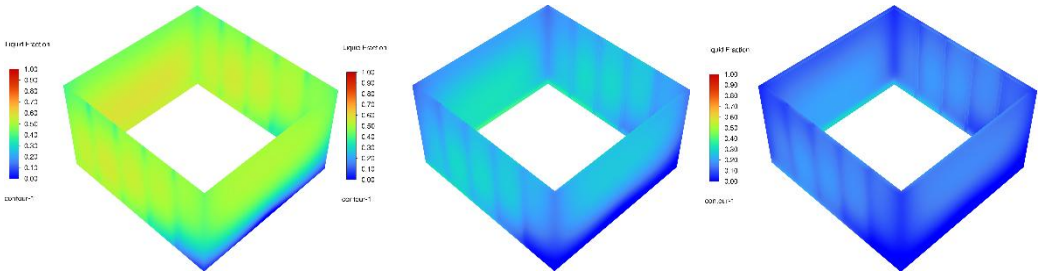
K. As the thickness of the PCM increases, both the maximum temperature and the maximum temperature difference of the battery pack decrease, but the decrease is very small. Compared with liquid cooling, phase change cooling contributes less to reducing the maximum temperature, but it makes a significant contribution to maintaining a uniform temperature distribution.



Maximum temperature Temperature difference

Fig. 10The maximum temperature and temperature difference of the battery at different PCM thickness

The liquid fraction of the PCM and the temperature cloud map is also shown in Fig. 11 and Fig. 12. As the thickness of the PCM increases, the temperature distribution of the battery pack becomes more uniform (the color of the cloud map is more consistent), but the liquid fraction of the PCM gets lower and lower, and the utilization rate decreases. Therefore, a thickness of 2 mm is more appropriate.



PCM thickness:1 mm 3 mm 4 mm

Fig. 11 LF contours for hybrid cooling at different thickness of PCM

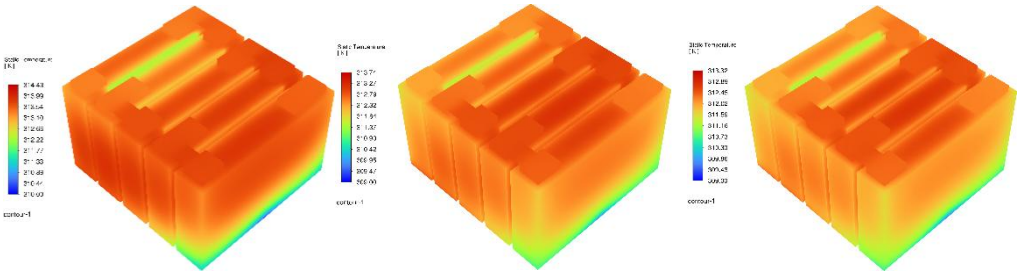


Fig. 12 The temperature cloud map at different PCM thickness

4 Conclusion

A hybrid cooling method with PCM and liquid cooling for lithium battery packs was proposed to improve the thermal performance of LIB battery pack. Under the hybrid cooling method, the battery pack was discharged at 3 C rate, with a maximum temperature of 313.31 K and a maximum temperature difference of 4.12 K, both reaching the optimal temperature range of the battery pack. Meanwhile, the influence of the cold plate setting arrangement, liquid flow velocity and PCM thickness were studied. The fence structure and the water flows in opposite directions can control the maximum temperature and the maximum temperature difference at 315.86 K and 5.78 K respectively. Meanwhile, the color of the temperature cloud map is more uniform. As the water flow increases, the maximum temperature drops and the temperature

difference widens. Considering factors such as pressure drop comprehensively, the flow rate is selected as 0.1 m/s. Liquid cooling has a higher heat dissipation capacity than PCM cooling, but the temperature uniformity of PCM cooling is better. As the thickness of PCM increases, both the maximum temperature and the maximum temperature difference decrease, but the liquid fraction of PCM reduces. Considering all factors, a thickness of 2 mm is selected.

Acknowledgements

This work was supported by the Natural Science Foundation of Wuhan (2025041001010356, 2024040701010057 & 2024010702030096), Technology Innovation Special Foundation of Hubei Province (2025AFA061), Hubei Provincial Teaching Reform Research Project for Graduate Education (2025670).

Reference

[1] Fan Y, Bao Y, Ling C, et al. Experimental study on the thermal management performance of air cooling for high energy density cylindrical lithium-ion batteries[J]. Applied Thermal Engineering, 2019, 155: 96-109.

[2] Aneke M, Wang M. Energy storage technologies and real life applications – A state of the art review[J]. Applied Energy, 2016, 179: 350-377.

[3] Abdelkareem M A, Maghrabie H M, Abo-Khalil A G, et al. Thermal management systems based on heat pipes for batteries in EVs/HEVs[J]. Journal of Energy Storage, 2022, 51: 104384.

[4] Yang X G, Liu T, Gao Y, et al. Asymmetric Temperature Modulation for Extreme

525 Fast Charging of Lithium-Ion Batteries[J]. Joule, 2019, 3(12): 3002-3019.
526 [5] Kong X, Zhang H, Du Y, et al. Topology optimization of thermal-fluid systems
527 with non-uniform thermal loads using a novel objective function[J]. International
528 Journal of Heat and Fluid Flow, 2025, 116: 109998.
529 [6] Wang S, Hu C, Yu R, et al. Study on low-temperature cycle failure mechanism of
530 a ternary lithium ion battery[J]. RSC Advances, 2022, 12(32): 20755-20761.
531 [7] Chen Z, Wang J, Huang J, et al. The high-temperature and high-humidity storage
532 behaviors and electrochemical degradation mechanism of LiNi0.6Co0.2Mn0.2O2
533 cathode material for lithium ion batteries[J]. Journal of Power Sources, 2017, 363: 168-
534 176.
535 [8] Wu W, Wu W, Wang S. Thermal management optimization of a prismatic battery
536 with shape-stabilized phase change material[J]. International Journal of Heat and Mass
537 Transfer, 2018, 121: 967-977.
538 [9] Wang Q, Jiang B, Li B, et al. A critical review of thermal management models and
539 solutions of lithium-ion batteries for the development of pure electric vehicles[J].
540 Renewable and Sustainable Energy Reviews, 2016, 64: 106-128.
541 [10] Saw L H, Ye Y, Tay A A O. Integration issues of lithium-ion battery into electric
542 vehicles battery pack[J]. Journal of Cleaner Production, 2016, 113: 1032-1045.
543 [11] Wang C H, Lin T, Huang J T, et al. Temperature response of a high power lithium-
544 ion battery subjected to high current discharge[J]. Materials Research Innovations,
545 2015, 19(sup2): S2-156-S2-160.

546 [12]Wu C, Sun Y, Tang H, et al. A review on the liquid cooling thermal management
547 system of lithium-ion batteries[J]. Applied Energy, 2024, 375: 124173.
548 [13]Pesaran A A. Battery Thermal Management in EVs and HEVs: Issues and
549 Solutions[J], Battery Man, 2001, 43.
550 [14]Zhou H, Zhou F, Zhang Q, et al. Thermal management of cylindrical lithium-ion
551 battery based on a liquid cooling method with half-helical duct[J]. Applied Thermal
552 Engineering, 2019, 162: 114257.
553 [15]Huang Y H, Cheng W L, Zhao R. Thermal management of Li-ion battery pack with
554 the application of flexible form-stable composite phase change materials[J]. Energy
555 Conversion and Management, 2019, 182: 9-20.
556 [16]Zou D, Liu X, He R, et al. Preparation of a novel composite phase change material
557 (PCM) and its locally enhanced heat transfer for power battery module[J]. Energy
558 Conversion and Management, 2019, 180: 1196-1202.
559 [17]Yuan Q, Xu X, Tong G, et al. Effect of coupling phase change materials and heat
560 pipe on performance enhancement of Li-ion battery thermal management system[J].
561 International Journal of Energy Research, 2021, 45(4): 5399-5411.
562 [18]Yang H, Zhang G, Dou B, et al. Review on the Lithium-Ion Battery Thermal
563 Management System Based on Composite Phase Change Materials: Progress and
564 Outlook[J]. Energy & Fuels, 2024, 38(4): 2573-2600.
565 [19]Cao J, Ling Z, Fang X, et al. Delayed liquid cooling strategy with phase change
566 material to achieve high temperature uniformity of Li-ion battery under high-rate

discharge[J]. Journal of Power Sources, 2020, 450: 227673.

[20] Yao F, Guan X, Chen Q, et al. Research on thermal management system of lithium-ion battery with a new type of spider web liquid cooling channel and phase change materials[J]. Journal of Energy Storage, 2024, 81: 110447.

[21] Zhou Z, Wang D, Peng Y, et al. Experimental study on the thermal management performance of phase change material module for the large format prismatic lithium-ion battery[J]. Energy, 2022, 238: 122081.

[22] Paul D, Nandi A, Bhattacharyya S, et al. A comprehensive review on lithium-ion battery thermal management (BTM) using phase change materials: advances, challenges, and future perspectives[J]. Journal of Thermal Analysis and Calorimetry, 2025, 150(12): 9669-9722.

[23] Chen D, Jiang J, Kim G H, et al. Comparison of different cooling methods for lithium ion battery cells[J]. Applied Thermal Engineering, 2016, 94: 846-854.

[24] Jarrett A, Kim I Y. Design optimization of electric vehicle battery cooling plates for thermal performance[J]. Journal of Power Sources, 2011, 196(23): 10359-10368.

[25] Liu R, Chen J, Xun J, et al. Numerical investigation of thermal behaviors in lithium-ion battery stack discharge[J]. Applied Energy, 2014, 132: 288-297.

[26] Wang Z, Wang X, Liang G, et al. Topology optimization design and thermofluid performance analysis of li-ion battery cooling plate[J]. Structural and Multidisciplinary Optimization, 2024, 67(11): 198.

[27] Zhan S, Liang L, Li Z, et al. Topology optimization of liquid cooling plate for

588 lithium battery heat dissipation based on a bionic leaf-vein structure[J]. International
589 Journal of Heat and Mass Transfer, 2024, 231: 125898.
590 [28]Liu J, Zhang X, Xi Y, et al. A comprehensive review of hybrid liquid and PCM
591 cooling BTMS[J]. Journal of Thermal Analysis and Calorimetry, 2025, 150(25): 20539-
592 20572.
593 [29]Zhang H, Wu X, Wu Q, et al. Experimental investigation of thermal performance
594 of large-sized battery module using hybrid PCM and bottom liquid cooling
595 configuration[J]. Applied Thermal Engineering, 2019, 159: 113968.
596 [30]Bai F, Chen M, Song W, et al. Thermal management performances of PCM/water
597 cooling-plate using for lithium-ion battery module based on non-uniform internal heat
598 source[J]. Applied Thermal Engineering, 2017, 126: 17-27.
599 [31]Ping P, Zhang Y, Kong D, et al. Investigation on battery thermal management
600 system combining phase changed material and liquid cooling considering non-uniform
601 heat generation of battery[J]. Journal of Energy Storage, 2021, 36: 102448.
602 [32]Gao Z, Deng F, Yan D, et al. Thermal performance of thermal management system
603 coupling composite phase change material to water cooling with double s-shaped
604 micro-channels for prismatic lithium-ion battery[J]. Journal of Energy Storage, 2022,
605 45: 103490.
606 [33]Zhuang Y, Chen T, Chen J, et al. Thermal uniformity performance of a hybrid
607 battery thermal management system using phase change material and cooling plates
608 arrayed in the manner of honeycomb[J]. Thermal Science and Engineering Progress,

609 2021, 26: 101094.

610 [34] Zhao Y, Zhang X, Yang B, et al. A review of battery thermal management systems

611 using liquid cooling and PCM[J]. Journal of Energy Storage, 2024, 76: 109836.

612 [35] Zhang F, Li X, Zhao H, et al. Symmetrical complex serpentine channel introduction

613 of secondary openings with open Y fins integrated optimization design[J]. International

614 Journal of Thermal Sciences, 2024, 195: 108620.

615 [36] Wang W, Shao Y, Tian Y, et al. Research on performance of liquid cooling plate for

616 topology optimization of lithium-ion battery[J]. International Journal of

617 Electrochemical Science, 2025, 20(11): 101175.

618 [37] Wang T, Hu H, Wang Y. Topological Approach for Optimization of Liquid Cooled

619 Plate with Different Inlet/Outlet Parameters[A]. SSRN, 2024.

620 [38] Gong M, Chen J, Chen J, et al. Study on Discharge Characteristic Performance of

621 New Energy Electric Vehicle Batteries in Teaching Experiments of Safety Simulation

622 under Different Operating Conditions[J]. Energies, 2024, 17(12): 2845.

623 [39] Wang Z, Zhu K, Hu J, et al. Study on the fire risk associated with a failure of large-

624 scale commercial $LiFePO_4$ /graphite and $LiNi_x\ Co_y\ Mn_{1-x-y}\ O_2$ /graphite batteries[J].

625 Energy Science & Engineering, 2019, 7(2): 411-419.

626 [40] Huang Z, Li X, Wang Q, et al. Experimental investigation on thermal runaway

627 propagation of large format lithium ion battery modules with two cathodes[J].

628 International Journal of Heat and Mass Transfer, 2021, 172: 121077.

629 [41] Ding Y, Cano Z P, Yu A, et al. Automotive Li-Ion Batteries: Current Status and

630 Future Perspectives[J]. Electrochemical Energy Reviews, 2019, 2(1): 1-28.
631 [42] Xu Y, Ren Q, Zheng Z J, et al. Evaluation and optimization of melting performance
632 for a latent heat thermal energy storage unit partially filled with porous media[J].
633 Applied Energy, 2017, 193: 84-95.
634 [43] Mubashir M, Xu J, Guo Z, et al. Experimental and numerical investigation of single
635 and double serpentine channel cold plates on the thermal performance of lithium ion
636 pouch battery[J]. Journal of Energy Storage, 2024, 92: 112200.
637 [44] Zheng H, Wang C, Liu Q, et al. Thermal performance of copper foam/paraffin
638 composite phase change material[J]. Energy Conversion and Management, 2018, 157:
639 372-381.
640 [45] Panchal S, Khasow R, Dincer I, et al. Thermal design and simulation of mini-
641 channel cold plate for water cooled large sized prismatic lithium-ion battery[J]. Applied
642 Thermal Engineering, 2017, 122: 80-90.
643 [46] Deng Y, Feng C, E J, et al. Effects of different coolants and cooling strategies on
644 the cooling performance of the power lithium-ion battery system: A review[J]. Applied
645 Thermal Engineering, 2018, 142: 10-29.
646 [47] Chein R, Chen J. Numerical study of the inlet/outlet arrangement effect on
647 microchannel heat sink performance[J]. International Journal of Thermal Sciences,
648 2009, 48(8): 1627-1638.

Supplementary Files

This is a list of supplementary files associated with this preprint. Click to download.

- supportinginformation.docx